A polarized ^{3}He system based on metastability-exchange optical pumping

Yuting Wang[1,2], Liangyong Wu[2,3], Kaiyuan Zhang[2,4], Mei Peng[2,4], Siyu Chen[2,4*], and Haiyang Yan[2,4*]

[1] *State Key Laboratory of Nuclear Physics and Technology, School of Physics, Peking University, Beijing 100871, China;*
[2] *Institute of Nuclear Physics and Chemistry, China Academy of Engineering Physics, Mianyang 621900, China;*
[3] *Key Laboratory of Nuclear Physics and Ion-beam Application (MOE), Fudan University, Shanghai 200433, China;*
[4] *Key Laboratory of Neutron Physics, Institute of Nuclear Physics and Chemistry, China Academy of Engineering Physics, Mianyang 621900, China*

Hyperpolarized ^{3}He nuclei have emerged as a significantly important approach in quantum precision measurement techniques, with extensive applications in fundamental physics, magnetometry, metrology, and beyond. In this study, we report on the design and implementation of a ^{3}He polarization system at the China Mianyang Research Reactor (CMRR), utilizing the metastability-exchange optical pumping (MEOP) method. We employed a Merritt coil system consisting of four square coils to furnish a uniform holding field. We deployed a 2 W fiber laser to pump the metastable ^{3}He atoms and conducted free induction decay (FID) detection of the polarized ^{3}He nuclei using both pickup coil and optical methods. For the optical method, we used a 50 mW linearly polarized distributed Bragg reflector (DBR) laser as the probe. We applied transverse light absorption polarimetry to measure the absolute nuclear polarization of the ground-state ^{3}He. We have developed cell fabrication capabilities at the CMRR, and cells at various pressures ranging from 100 to 1000 Pa have been fabricated and evaluated. For a typical borosilicate cell with 100 Pa pressure, the absolute polarization is measured as $P_n \approx 70\%$, and the transverse relaxation time is estimated as $T_2 \approx 0.5$ s. Moreover, we constructed a few aluminosilicate cells, each carefully filled with pure ^{3}He at a pressure of 100 Pa. Subsequently, we conducted a comprehensive evaluation of their performance in the context of MEOP.

1 Introduction

Hyperpolarized ^{3}He gas has been extensively applied in diverse fields. It acts as a sensitive probe for weak magnetic fields in fundamental physics, aiding investigations into new physics beyond the Standard Model [1]. More specifically, it is instrumental in the search for spin-dependent exotic interactions [2-8] and the precise measurement of the electric dipole moment of an atom or a neutron [9-13]. In the realm of medical science, hyperpolarized ^{3}He or other species of noble gas are used as a contrast agent for nuclear magnetic resonance imaging, offering substantial potential for enhancing our capacity to perform both morphological and functional analyses of the lung [14-17]. This relevant technique, utilizing ^{129}Xe, has even assisted in the diagnosis of lung and brain injuries resulting from COVID-19 [18, 19]. The polarized ^{3}He system serves as a neutron spin filter or analyzer in neutron scattering experiments. As a state-of-the-art technique for polarizing and analyzing neutrons, it has been successfully implemented into spectrometers at various neutron

sources globally [20-27].

Generally, two methods are used to polarize ^{3}He [28]: spin-exchange optical pumping (SEOP) [29] and metastability-exchange optical pumping (MEOP) [30]. The SEOP method relies on the gradual transfer of electronic polarization from alkali atoms to the ^{3}He nucleus via spin-exchange collisions, with alkali atoms being polarized through optical pumping. This process necessitates an oven to vaporize the alkali metals, maintaining a typical temperature of 170°C for Rb cells and 240°C for Rb-K mixed cells [31, 32]. In 2019, a ^{3}He polarizing device utilizing the SEOP method was established at the China Mianyang Research Reactor (CMRR) [33]. This marked the first development of such a system in China for neutron polarization analysis in a spin-echo spectrometer. In the MEOP method, electron polarization is produced within metastable ^{3}He atoms via optical pumping and then transfers to the ground-state population through metastability exchange collisions (MECs). Unlike SEOP, the MEOP approach does not require heating, resulting in minimal temperature-related effects. Moreover, MEOP begins with a rate constant nearly nine orders of magnitude larger than that of SEOP, demonstrating its superior efficiency in achieving ^{3}He polarization. As a result, numerous MEOP-based hyperpolarized ^{3}He applications have been implemented in fundamental physics research and national defense initiatives [34-37]. For example, MEOP-based ^{3}He polarizing systems have been used to explore the transferred spin-dressing effect in ^{3}He atoms, and both the triplet and quintuplet spectra have been observed [34]. Absolute magnetometry using polarized ^{3}He based on the MEOP technique has made significant advancements in recent years and is now considered a new standard in the field [35, 38]. This is of considerable importance for applications in precision experiments, such as the muon *g*-2 experiments at Fermilab and J-PARC [39, 40].

In this study, we present the implementation of a ^{3}He polarization system based on the MEOP method at the CMRR. A Merritt coil system, composed of four square coils, was used to provide a uniform holding field. We utilized a 2 W fiber laser to pump the metastable ^{3}He atoms. Free induction decay (FID) detection of the polarized ^{3}He nuclei was carried out using both pickup coil and optical methods. For the optical method, a 50 mW linearly polarized distributed Bragg reflector (DBR) laser was employed as the probe. We applied transverse light absorption polarimetry [41] to measure the absolute nuclear polarization of the ground-state ^{3}He. Furthermore, we have established cell fabrication capabilities at CMRR. As such, more than ten cells at various pressures ranging from 100 to 1000 Pa have been successfully fabricated and tested.

This paper is structured as follows. The MEOP method and optical magnetometry are introduced in sect. 2. Details of our apparatuses, including the pumping optics and the experimental setup for polarization measurement, are presented in sect. 3. The results are shown and discussed in sect. 4. A summary and some prospects are given in sect. 5.

## 2 MEOP basics

2.1 Fundamental processes for polarizing ^{3}He

MEOP involves two key processes: optical pumping (OP) and metastability-exchange collisions. The relevant energy levels of a ^{3}He atom are schematically represented in Figure 1. A weak radio frequency (RF) discharge excites a small fraction (approximately 10^{-6}) of the ^{3}He atoms to their metastable states (2^3S_1). The C8 line, when circularly (σ_+) polarized, can be used to pump these ^{3}He atoms from the $|F = \frac{1}{2}, m_F = -\frac{1}{2}\rangle$ state of 2^3S_1 to the $|F = \frac{1}{2}, m_F = \frac{1}{2}\rangle$ state of 2^3P_0. Subsequently, the atoms decay back to the 2^3S_1 state through spontaneous emission; this transition occurs with well-defined branching ratios. As a result, the ^{3}He atoms are primarily enriched in the $|F = \frac{1}{2}, m_F = \frac{1}{2}\rangle$ state of 2^3S_1, resulting in polarized atoms in the metasable state.

The polarization of ^{3}He atoms in the ground state is achieved via MECs with polarized metastable ^{3}He atoms. This process effectively transfers polarization from the metastable state to the ground state in a very short time (10^{-12} s), with negligible spin depolarization during the collision [42]. This property is attributed to the fact that all involved angular momenta are spins. It also enforces a Boltzmann-like distribution in angular momentum for the relative populations of all sublevels coupled by MECs, resulting in a spin-temperature distribution. The populations of the metastable Zeeman sublevels scale exponentially with their respective angular momentum, with a Boltzmann parameter defined as $e^\beta = (1 + P)/(1 - P)$, where P represents the polarization of ground-state ^{3}He [12, 43].

The polarization of the ^{3}He atoms in the metastable state can be assessed through light absorption measurements, which allows for determining the polarization of ground-state ^{3}He [41, 44, 45]. Additional methods for probing the polarization of ^{3}He during MEOP include fluorescence light polarimetry [46] and nuclear magnetic resonance measurements [47].

2.2 Magnetic resonance in ground and metastable states

The magnetic resonance of ^{3}He atoms is achieved by applying an RF field, $B_1\cos(\omega t)\hat{x}$, perpendicular to the hold-
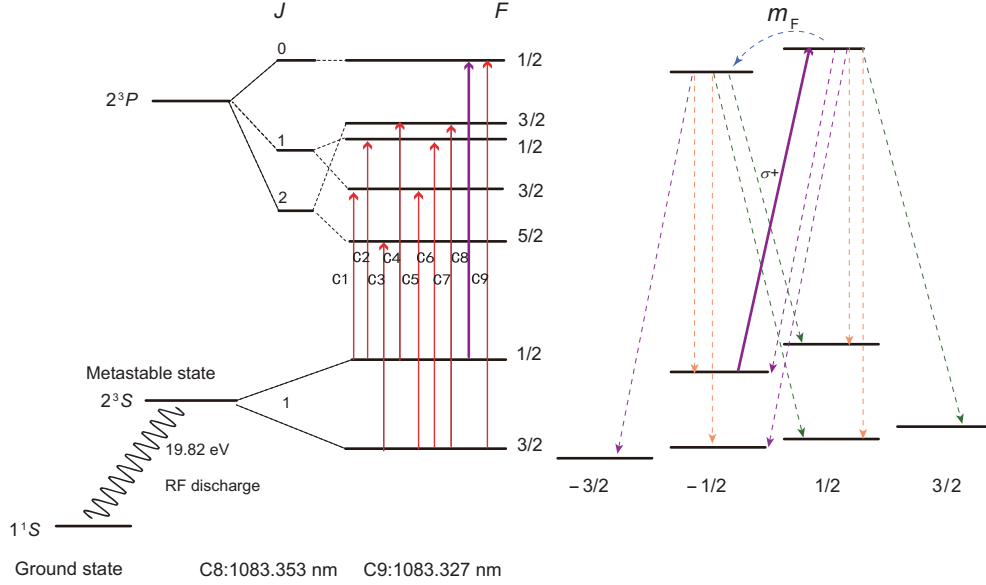
Figure 1   (Color online) Diagram of ^{3}He atomic energy levels (not to scale) at the low magnetic field, illustrating the levels involved in the MEOP process.

ing field, $B_0\hat{z}$. The Bloch equation describes the evolution of the angular momentum in the presence of the fields [48]. In MEOP, the magnetic resonances of the ground and metastable states are coupled through MECs. In a rotating frame that revolves around the $\hat{z}$ axis at a frequency ω, the evolution of the angular momenta can be expressed as follows [34, 49]:

$$
\begin{aligned}
\frac{\partial}{\partial t}\langle \mathbf{I}\rangle_g &= \langle \mathbf{I}\rangle_g \times \left[(\omega_n - \omega\hat{z}) + \gamma_n B_1\hat{x}\right] - \Gamma_g\langle \mathbf{I}\rangle_g \\
&\quad + \frac{1}{T_e}\left[-\langle \mathbf{I}\rangle_g + \frac{1}{3}\langle \mathbf{F}\rangle_{\frac{3}{2}} - \frac{1}{3}\langle \mathbf{F}\rangle_{\frac{1}{2}}\right], \\
\frac{\partial}{\partial t}\langle \mathbf{F}\rangle_{\frac{3}{2}} &= \langle \mathbf{F}\rangle_{\frac{3}{2}} \times \left[\left(\frac{2}{3}\omega_e - \omega\hat{z}\right) + \gamma_{\frac{3}{2}} B_1\hat{x}\right] - \Gamma_e\langle \mathbf{F}\rangle_{\frac{3}{2}} \\
&\quad + \frac{1}{\tau_e}\left[-\frac{4}{9}\langle \mathbf{F}\rangle_{\frac{3}{2}} + \frac{10}{9}\langle \mathbf{I}\rangle_g + \frac{10}{9}\langle \mathbf{F}\rangle_{\frac{1}{2}}\right], \\
\frac{\partial}{\partial t}\langle \mathbf{F}\rangle_{\frac{1}{2}} &= \langle \mathbf{F}\rangle_{\frac{1}{2}} \times \left[\left(\frac{4}{3}\omega_e - \omega\hat{z}\right) + \gamma_{\frac{1}{2}} B_1\hat{x}\right] - \Gamma_e\left(\langle F_z\rangle_{\frac{1}{2}} - P\hat{z}\right) \\
&\quad + \frac{1}{\tau_e}\left[-\frac{7}{9}\langle \mathbf{F}\rangle_{\frac{1}{2}} - \frac{1}{9}\langle \mathbf{I}\rangle_g + \frac{1}{9}\langle \mathbf{F}\rangle_{\frac{3}{2}}\right],
\end{aligned}
\tag{1}
$$

where ω_n and ω_e denote the Larmor frequencies of the nucleus and the electron, respectively. The relaxation rates of the ground state and metastable state are represented by Γ_g and Γ_e, respectively. The mean free time of MECs for the ground and metastable states are given by T_e and τ_e, respectively. The gyromagnetic ratios for the ground and metastable states are denoted by γ_n, $\gamma_{\frac{3}{2}}$, and $\gamma_{\frac{1}{2}}$, respectively. The parameter P characterizes the atomic polarization induced by optical pumping. Typical values for the parameters in eq. (1) are: $T_e \sim 1$ s, $\tau_e \sim 10^{-6}$ s, $\Gamma_e \sim 10^3$ s^{-1}, and $\Gamma_g \sim 1$ s^{-1}.

The pump laser is aligned with the holding field, causing the angular momentum's initial orientation along the $\hat{z}$ axis. The solution to eq. (1) can be derived based on the order of τ_e/T_e [50]. When the RF field is applied close to the resonance of the ground-state splitting ω_n, under the specific conditions of this study, we can adequately describe the transverse excitation as follows [50]:

$$
\begin{aligned}
\langle I_+\rangle(t) &= \frac{\langle I_z\rangle}{(\omega - \omega_n) + \mathrm{i}\left(\frac{1}{T_e} + \Gamma_g\right)}\frac{\gamma_n B_1}{2}\mathrm{e}^{-\mathrm{i}\omega t}, \\
\langle F_+\rangle_{\frac{1}{2}}(t) &= \frac{1}{9}\left[-\frac{2}{1 + \mathrm{i}\omega_e\tau_e} + \frac{5}{1 + 4\mathrm{i}\omega_e\tau_e}\right]\langle I_+\rangle(t), \\
\langle F_+\rangle_{\frac{3}{2}}(t) &= \frac{10}{9}\left[\frac{1}{1 + \mathrm{i}\omega_e\tau_e} + \frac{2}{1 + 4\mathrm{i}\omega_e\tau_e}\right]\langle I_+\rangle(t),
\end{aligned}
\tag{2}
$$

where $I_+ = I_x + \mathrm{i}I_y$ and $F_+ = F_x + \mathrm{i}F_y$. The first equation in eq. (2) characterizes the magnetic resonance of the ground state with a linewidth of $1/T_e + \Gamma_g$. The second and third equations in eq. (2) indicate the transverse excitations of the metastable states caused by the excitation of the ground state. Without the MECs ($\tau_e \to \infty$), the metastable state would not respond to the excitation of the ground state. When the applied RF field frequency is close to the resonance of the $F = \frac{1}{2}$ or $F = \frac{3}{2}$ state of 2^3S_1, the corresponding transverse excitations are as follows:

$$
\begin{aligned}
\langle F_+\rangle_{\frac{1}{2}}(t) &= \frac{\frac{\gamma_{\frac{1}{2}} B_1}{2}\langle F_z\rangle_{\frac{1}{2}}}{\left(\omega - \frac{4}{3}\omega_e\right) + \mathrm{i}\frac{7}{9\tau_e}}\mathrm{e}^{-\mathrm{i}\omega t}, \\
\langle F_+\rangle_{\frac{3}{2}}(t) &= \frac{\frac{\gamma_{\frac{3}{2}} B_1}{2}\langle F_z\rangle_{\frac{3}{2}}}{\left(\omega - \frac{2}{3}\omega_e\right) + \mathrm{i}\frac{4}{9\tau_e}}\mathrm{e}^{-\mathrm{i}\omega t}.
\end{aligned}
\tag{3}
$$

It can be seen that the magnetic resonance linewidth is $7/(9\tau_e)$ for the $F = \frac{1}{2}$ state and $4/(9\tau_e)$ for the $F = \frac{3}{2}$ state.

If an RF pulse of length τ is applied at resonance, the FID of the nuclear spin can be described as follows:

$$\langle I_+ \rangle(t) = i\frac{\gamma_n B_1 \tau}{2}\langle I_z \rangle e^{[-i\omega_n - (\frac{1}{T_e} + \Gamma_g)]t}. \quad (4)$$

In this case, the coupling of the metastable states to the ground state still follows eq. (2). As a result, we can achieve optical detection of the nuclear signal from the ground state. Additionally, by switching off the discharge, we can eliminate the $1/T_e$ term of the relaxation due to MECs. This action leads to the measurement of a longer transverse time T_2 with the pickup coil method.

2.3   Optical detection of magnetic resonance

Since the metastable state is optically accessible, magnetic resonance can be detected via Faraday rotation [51,52]. Faraday rotation refers to the phenomenon where the polarization of linearly polarized light rotates as it passes through a medium with a magnetic field that aligns with its direction of propagation. This metastable ^{3}He will induce different refractive indices for the left- and right-handed circularly polarized lights propagating along the field direction, consequently causing a rotation of the polarization of the linearly polarized light. For an off-resonance linearly polarized light propagating along the $\hat{x}$ axis, the rotation angle of the polarization after passing through a cell containing polarized metastable ^{3}He is given as [51,53]:

$$\phi = \frac{nr_e f_{em}cl}{2}$$
$$\times \left[2\langle F_x \rangle_\frac{1}{2}\frac{\nu - \nu_\frac{1}{2}}{(\nu - \nu_\frac{1}{2})^2 + \Gamma^2} + \langle F_x \rangle_\frac{3}{2}\frac{\nu - \nu_\frac{3}{2}}{(\nu - \nu_\frac{3}{2})^2 + \Gamma'^2}\right], \quad (5)$$

where n represents the number density of the metastable ^{3}He, r_e is the classical electron radius, f_{em} is the oscillator strength, c is the speed of light, and l is the propagation distance. The transition frequency of C8 (C9) is denoted by $\nu_\frac{1}{2}$ ($\nu_\frac{3}{2}$), Γ (Γ') is the linewidth of C8 (C9), ν is the center frequency of the probe light and $\langle F_x \rangle_\frac{1}{2}$ ($\langle F_x \rangle_\frac{3}{2}$) represents the angular momentum projection on the light propagation direction. At a low magnetic field (approximately 10 G), the $F = \frac{1}{2}$ and $F = \frac{3}{2}$ hyperfine levels of 2^3S_1 are split by approximately 6.74 GHz and are well resolved [28]. As a result, the magnetic resonances on these two levels can be observed individually. As demonstrated in sect. 2.2, the magnetic resonance on the ground state can be deduced from those on the $F = \frac{1}{2}$ and $F = \frac{3}{2}$ hyperfine levels of 2^3S_1 with the help of eq. (2). Therefore, the magnetic resonance of the ground state can be observed through those metastable states, which are measured optically through Faraday rotation.

3   Experimental setup

The schematic diagram of the experimental apparatus is illustrated in Figure 2. A square Merritt coil provides a holding magnetic field of approximately 10 G in the z direction. An atomic cell with a cylindrical shape (dimensions: $\phi = 50$ mm, $L = 50$ mm), made from borosilicate glass and filled with pure ^{3}He (pressure: approximately 100 Pa), is positioned at the center of the Merritt coil. All cells used in our experiments are fabricated in our laboratory, involving processes such as glassblowing, rinsing, gas-filling, and sealing. Figure 3 showcases some of the borosilicate cells we have fabricated. A pair of copper rings, attached to the cell's surface, is connected to an RF power generator to sustain the discharge of ^{3}He.

The optical pumping of ^{3}He is achieved using a Ytterbium-doped fiber laser, which features a linewidth of approximately 2 GHz and a maximum output power of 20 W. This laser can be tuned to ^{3}He transitions from C3 to C9, making it suitable for Helium pumping and spectroscopy. Before entering the cell, the laser light is circularly polarized using a combination of a polarizing beamsplitter (PBS) and a quarter-wave plate (QWP). The light reflected off the PBS is directed into a wavelength meter, which provides feedback for stabilizing the center frequency. The half-wave plate (HWP) is situated before the PBS adjusts the proportion between reflected and transmitted power. The light beam diameter is expanded to match the size of the cell. The laser propagates parallel to the holding field, accumulating ^{3}He
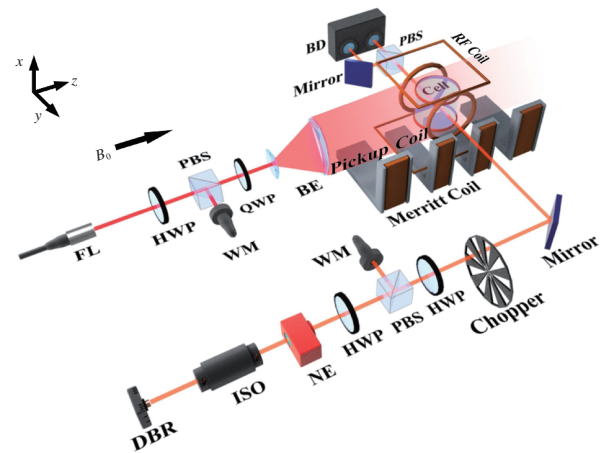
Figure 2   (Color online) Schematic diagram of the experimental setup. Key components include: FL, fiber laser (pumping light); HWP, half-wave plate; PBS, polarizing beamsplitter; QWP, quarter-wave plate; WM, wavelength meter; BE, beam expander; PD, photoelectric detector; DBR, distributed Bragg reflection laser (probe light); ISO, optical isolator; NE, noise eater; BD, balanced detector. The cell is illuminated by copper rings using radio frequency signals in the megahertz range. A square Merritt coil generates the primary magnetic field B_0 along the $\hat{z}$ axis, while a pair of RF coils provide the transverse field.
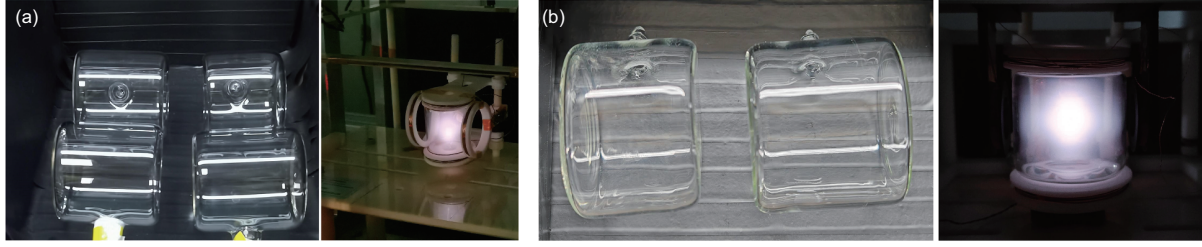
Figure 3   (Color online) (a) Atomic cells fabricated in our lab using borosilicate glass at various pressures (left) and a cell undergoing discharge (right). (b) Atomic cell fabricated in our lab using aluminosilicate glass at a pressure of 100 Pa (left) and a cell undergoing discharge (right).

polarization in the same direction.

The probe light is radiated by a DBR laser diode with a maximum output power of approximately 50 mW. The center wavelength can be adjusted by varying its temperature. The light beam emitted from the DBR is divergent, which necessitates a beam collimator (not shown in Figure 2) to be positioned between the DBR and the optical isolator (ISO) for collimation. A noise eater (NE) is utilized to maintain the stability of the light power. A HWP placed after the PBS can be used to modify the polarization of the light. The probe light propagates in the y direction, which is perpendicular to the main field. We utilize a differential detection scheme to measure the rotation angle of the probe light. The balanced detector (BD) output is proportional to the rotation angle. In our experiment, RF pulses for driving FID are generated digitally, and a lock-in amplifier is used to detect the signal.

4   Results

Initially, a holding field of approximately 10 G is generated by the Merritt coils, and a pair of coils radiate RF pulses along the $\hat{x}$ axis to realize the FID NMR for the ground state. The probe light, red detuned about 2 GHz off the C9 transition, is used to measure the magnetic resonance. The signal acquired from the BD is demodulated by sweeping reference frequencies across the resonance. The experimental results are represented by blue circles in Figure 4, along with the fitted results displayed by a red dashed line. The frequency at resonance is determined to be $f_0 = 34021.06 \pm 0.02$ Hz, corresponding to a magnetic field of $B_0 = 2\pi f_0/\gamma_n = (10.5 \pm 6.2 \times 10^{-6})$ G. The obtained resonance linewidth is $\Delta = 1.06 \pm 0.04$ Hz, indicating a relaxation rate of $\Gamma_g = 2\pi\Delta = 6.68 \pm 0.26$ s^{-1} for the ground-state ^{3}He.
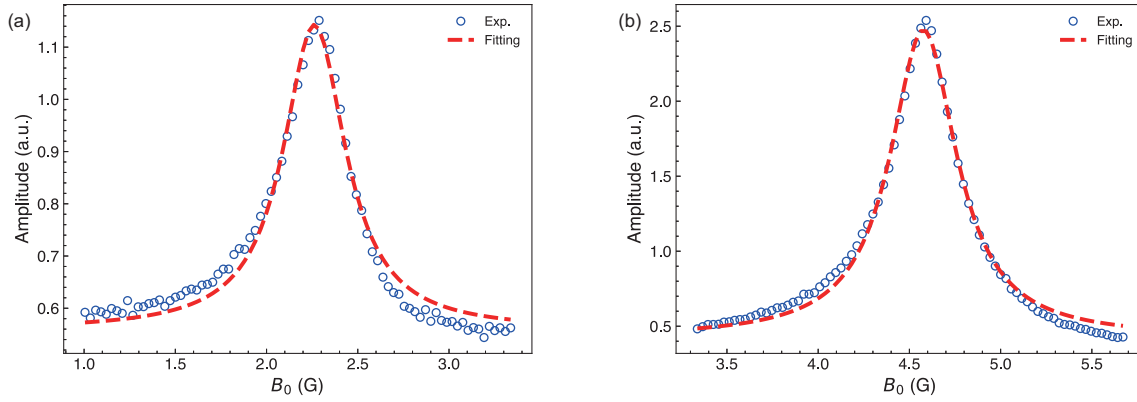
Next, the frequency of the RF field is adjusted to $\omega = 8.6$ MHz to realize the magnetic resonance of the metastable states—this time, the signal is demodulated to reference frequencies corresponding to different holding field strengths. The obtained results for the $F = \frac{1}{2}$ and $F = \frac{3}{2}$ states are displayed in Figure 5(a) and (b), respectively, with the dashed

lines representing the fitted results. The holding field at resonance for the $F = \frac{1}{2}$ and $F = \frac{3}{2}$ states is $B_0 = 2.262 \pm 0.004$ G and $B_0 = 4.576 \pm 0.002$ G, respectively. These correspond to the resonance frequencies of $\omega_{\frac{1}{2}} = \gamma_{\frac{1}{2}} B_0 = 8.596 \pm 0.015$ MHz and $\omega_{\frac{3}{2}} = \gamma_{\frac{3}{2}} B_0 = 8.694 \pm 0.004$ MHz. The extracted linewidth of the resonance is $\Delta_{\frac{1}{2}} = 0.789 \pm 0.031$ MHz for the $F = \frac{1}{2}$ state and $\Delta_{\frac{3}{2}} = 0.421 \pm 0.009$ MHz for the $F = \frac{3}{2}$ state. This discrepancy may be due to the coherence between $F = \frac{1}{2}$ and $F = \frac{3}{2}$ state caused by the MECs when the magnetic field is not high enough to discriminate the magnetic resonance between them [50]. The MECs time derived from the linewidth is $\tau_e = (1.02 \pm 0.02) \times 10^{-6}$ s.

Traditionally, the FID signal can be detected using a pickup coil, which detects the RF field radiated by precessions of magnetic moments. On the other hand, under the MEOP conditions, the FID signal can also be accessed with an optical method. Both of these methods were adopted in our experiments, and the detected FID signals are presented respectively in Figure 6(a) and (c), with the corresponding spectra from fast Fourier transform (FFT) displayed in Figure 6(b) and (d). The blue circles denote the output of the lock-in amplifier, where the reference frequency is set to be
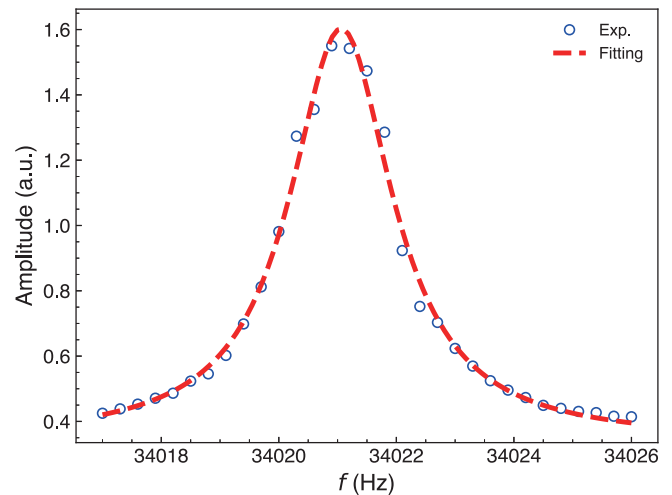
Figure 4   (Color online) The magnetic resonance curve of the ground state ^{3}He. The holding field is approximately 10 G, and the frequency of the RF field gradually sweeps through the resonance. The blue circles represent the demodulated signal, and the red dashed line depicts the fitted result.

Figure 5   (Color online) The magnetic resonance curve of the metastable state ^{3}He. The frequency of the RF field is fixed to $\omega = 8.6$ MHz, and the holding field sweeps slowly through the resonance value. (a) The magnetic resonance of $F = \frac{1}{2}$ with the gyromagnetic ratio of $\gamma_{\frac{1}{2}} = 2\pi \times 3.8$ MHz/G. (b) The magnetic resonance of $F = \frac{3}{2}$ with the gyromagnetic ratio of $\gamma_{\frac{3}{2}} = 2\pi \times 1.9$ MHz/G. The blue circles are the demodulated signal, and the red dashed lines are the fitted result.
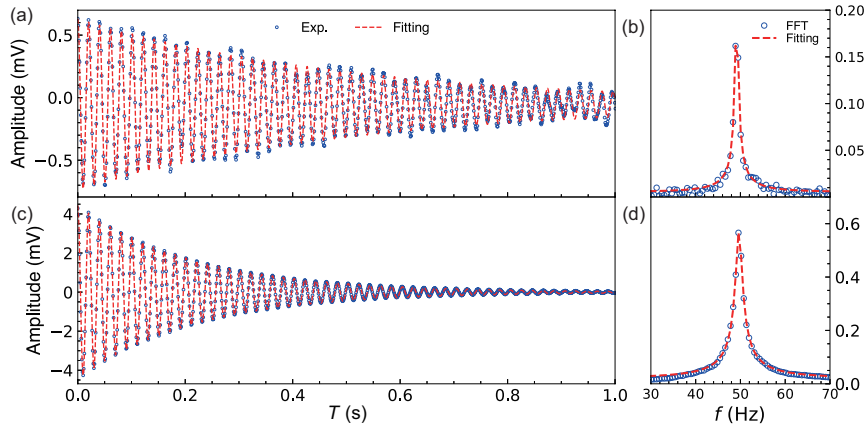

Figure 6   (Color online) FID signal from polarized ^{3}He is observed within an atomic cell under a pressure of 100 Pa. (a) The pickup coil detects the FID signal when the discharge is turned off. (c) The probe light detects the FID signal. Blue circles are the demodulated experimental data, and red dashed lines are the fitted results. (b) and (d) display the corresponding FFT spectra of (a) and (c).

50 Hz off-resonance of the ground-state ^{3}He, as observed at the peaks in Figure 6(b) and (d). The red dashed lines represent the fitted results. For Figure 6(a) and (c), the data were fitted using eq. (4), while the data in Figure 6(b) and (d) were fitted to the Lorentzian shape. The obtained relaxation time using the pickup coil method is found to be 524.1 ± 4.3 ms, corresponding to a half width at half maximum (HWHM) of 1.98 ± 0.18 Hz for the FFT spectrum in Figure 6(b). The relaxation time using the optical method is observed to be 217.5 ± 0.3 ms, corresponding to the HWHM of 4.55 ± 0.16 Hz in Figure 6(d). According to eq. (4), the transverse relaxation time is given by $T_2 = 1/(\frac{1}{T_e} + \Gamma_g)$. In our experimental study, we have observed a typical value of T_2 to be approximately 1 s, which is consistent with the theoretical prediction. The MECs time of the ground state is found to be $T_e = 0.37 \pm 0.01$ s (c.f. eq. (4)). The accurate determination of the resonance frequency is crucial for measuring the magnetic field. The statistical error of the frequency of the FID signal can be estimated by the Cramer-Rao lower bound as $\delta f^2 \geq 8/(4\pi^2 \mathrm{SNR}^2 T_2^3 f_{\mathrm{BW}})$ [54]. The calculated lower bound of the error is $\delta f = 0.12$ Hz in the optical method and $\delta f = 0.05$ Hz in the pickup coil method.

Light absorption polarimetry can determine the absolute polarization of ^{3}He [41]. The optical detection setup is shown in Figure 2. The linearly polarized light can be decomposed into two components, ε_z (polarization along B_0) and ε_x (polarization perpendicular to B_0). The absorption coefficient A of these components defines a ratio, $r = A_z/A_x$, which can be used to estimate the polarization of the ground-state ^{3}He as $P_n = \sqrt{(1 - r)/(1 + 2r)}$ for weak holding fields. The absorption signal is modulated at 320 Hz by a chopper, and lock-in detection is utilized to enhance SNR. Figure 7 displays the variation of P_n versus time in a typical pumping and relaxation cycle for a 100 Pa cell. We started to pump ^{3}He at the end of Region (1), a few seconds after turning on the measurement system; the polarization buildup process is
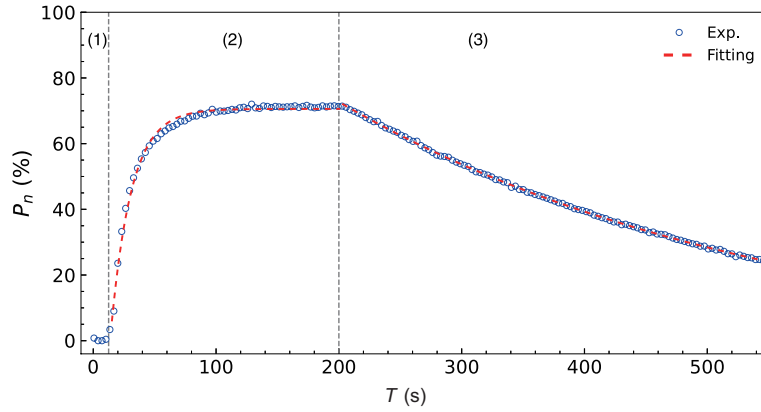
Figure 7 (Color online) Variation in polarization during a typical pump and relaxation cycle in a ^{3}He atomic cell at a pressure of 100 Pa. The blue circles represent the demodulated signal, and the red dashed line depicts the fitted result. The pump light is turned on at 20 s to polarize the ^{3}He and turned off at 200 s to facilitate the observation of polarization relaxation.

illustrated in Region (2), and in Region (3), the pump light is blocked off, and the polarization relaxation process begins. Fitting the results in Region (2) using $P_n(1 - e^{-t/T_p})$ and in Region (3) using $P_n e^{-t/T_1}$, one could derive the polarization P_n, the polarization buildup time T_p, and the longitudinal relaxation time T_1. A polarization of (70.57% ± 0.15%) is obtained, and the buildup time and the relaxation time are respectively $T_p = 16.7 ± 0.3$ s and $T_1 = 358.5 ± 3.4$ s. The longitudinal relaxation time, as derived from eq. (1) and referenced in ref. [50], is given by $T_1 = 1/(\Gamma_g + \frac{11n}{3N}\Gamma_e)$, where n and N represent the number density of metastable and ground-state ^{3}He atoms, respectively. The typical ratio of n/N is on the order of 10^{-6}. Therefore, based on this calculation, the expected value of T_1 is approximately 10^3 s, which aligns with our experimental result.

It is found that a weaker discharge can result in a longer relaxation time. The exact measurements were performed for all other cells with different pressures. We observed that the polarization decreases with increasing cell pressure, which is consistent with the findings in ref. [28]. Compared with borosilicate glass, aluminosilicate glass offers advantages such as lower magnetic impurities and permeability to ^{3}He atoms, making it more suitable for gaseous ^{3}He polarization. In the SEOP method, a cell made of aluminosilicate glass has been known since the 1970s to obtain higher polarization of ^{3}He and longer relaxation time. Recently, we fabricated a cylindrical cell using aluminosilicate glass and filled it with pure ^{3}He at a pressure of 100 Pa. Due to the challenges in processing aluminosilicate glass, we were only able to successfully fabricate a limited number of cells. We conducted preliminary tests on this cell to evaluate its performance for MEOP. The obtained saturated ^{3}He polarization was approximately (61.4% ± 1.6%), indicating comparable polarization to cells made of borosilicate glass. Furthermore, the longitudinal relaxation time, T_1, of the aluminosilicate

glass cell was measured to be 332 ± 14 s, which is also comparable to borosilicate glass. Additionally, the transverse relaxation time, T_2, of the FID signal with the discharge off was determined to be approximately 426.6 ± 2.5 ms. For the pickup coil method, we measured an SNR of 55, whereas for the optical method, the SNR reached 120.

5 Conclusion and prospects

In conclusion, a hyperpolarized ^{3}He system has been successfully established using the MEOP technique. This method is especially efficient for polarizing ^{3}He at lower pressures (around 100 Pa), with a typical pump-up time of approximately 20 s. The rapid preparation time is a significant advantage of MEOP over SEOP, as the latter typically requires about 10 h to pump up. Another benefit of MEOP is its independence from heating, making it more resistant to temperature fluctuations. We applied transverse light absorption polarimetry to measure the absolute polarization of ^{3}He. For the borosilicate cells, the highest polarization of ^{3}He at 100 Pa was observed to be (70.57% ± 0.15%), with a decrease in polarization as the pressure increases. The magnetic resonance on the ground and metastable states of ^{3}He was detected using both optical and pickup coil methods. For the ground state, we observed T_1 as long as 360 s and T_2 of 0.2 s when the discharge was on. When the discharge was off, the pickup coil method was used, resulting in a lower SNR (of 34 compared with that of 135 by the optical method) but a longer T_2 of 0.5 s. Furthermore, we fabricated a few aluminosilicate cells, each meticulously filled with pure ^{3}He at a pressure of 100 Pa. We then rigorously evaluated their performance with respect to MEOP processes. Although we did not observe a significant improvement with aluminosilicate glass in our tests, extensive research indicates that it

has significantly lower helium permeability, by several orders of magnitude, compared to borosilicate glass [55]. This helium-tight characteristic is considered crucial in achieving long-term stability and performance in certain specialized applications. These results highlight the potential advantages of using aluminosilicate glass for improving ^{3}He polarization and relaxation properties. Additional studies and refinements are required to thoroughly utilize the benefits of the two kinds of glass in real-world applications[1].

MEOP has shown to be an appropriate method for preparing hyperpolarized nuclei for atomic magnetometers. Recently, a Tesla magnetic field calibration to 32 parts per billion (ppb) was achieved using an absolute ^{3}He magnetometer based on MEOP [35]. The recent progress in accurately measuring the nuclear g factor of ^{3}He$^+$ has paved the way for ^{3}He to be established as an independent standard for absolute and precise magnetometry [38]. The optimal operating conditions for a low-field magnetometer, which relies on detecting the free spin precession of ^{3}He and ^{129}Xe, are achieved at a gas pressure of approximately 100 Pa [56]. This aligns with the pressure requirements for MEOP.

Creating nonclassical states of atomic ensembles, such as squeezed and entangled states, is essential for quantum precision measurements or quantum information [57, 58]. Most studies on nonclassical states focus on electrons [59, 60] due to their easy interaction with light. However, the complex interaction between electrons and their environment can shorten the lifetime of the quantum state. In contrast, a relatively isolated nucleus may offer advantages if the complexities of control and measurement can be overcome. The spin-exchange collision between electrons and nucleons has been experimentally validated as a method for controlling and measuring nuclei [61, 62]. Recently, MECs have been proposed as a potential method for manipulating the ^{3}He nucleus, enabling nuclear squeezing [63]. Given the speed of MECs compared to the spin-exchange collision, quantum manipulation of the nucleus based on MECs may offer increased efficiency. All these points underscore the promising potential of hyperpolarized ^{3}He, based on MEOP, in quantum precision measurement techniques.

Conflict of interest   The authors declare that they have no conflict of interest.

1 M. S. Safronova, D. Budker, D. DeMille, D. F. J. Kimball, A. Derevianko, and C. W. Clark, Rev. Mod. Phys. **90**, 025008 (2018), arXiv: 1710.01833.

2 L. Y. Wu, K. Y. Zhang, M. Peng, J. Gong, and H. Yan, Phys. Rev. Lett. **131**, 091002 (2023).

3 K. Y. Wu, S. Y. Chen, G. A. Sun, S. M. Peng, M. Peng, and H. Yan, Phys. Rev. Lett. **129**, 051802 (2022), arXiv: 2109.13847.

4 P. H. Chu, Y. J. Kim, and I. Savukov, Phys. Rev. D **94**, 036002 (2016), arXiv: 1606.01152.

5 H. Yan, G. A. Sun, S. M. Peng, Y. Zhang, C. Fu, H. Guo, and B. Q. Liu, Phys. Rev. Lett. **115**, 182001 (2015), arXiv: 1412.8155.

6 H. Yan, G. A. Sun, J. Gong, B. B. Pang, Y. Wang, Y. W. Yang, J. Zhang, and Y. Zhang, Eur. Phys. J. C **74**, 3088 (2014), arXiv: 1407.5828.

7 A. Arvanitaki, and A. A. Geraci, Phys. Rev. Lett. **113**, 161801 (2014), arXiv: 1403.1290.

8 P. H. Chu, A. Dennis, C. B. Fu, H. Gao, R. Khatiwada, G. Laskaris, K. Li, E. Smith, W. M. Snow, H. Yan, and W. Zheng, Phys. Rev. D **87**, 011105 (2013), arXiv: 1211.2644.

9 R. Picker, JPS Conf. Proc. **13**, 010005 (2017).

10 W. Zheng, H. Gao, B. Lalremruata, Y. Zhang, G. Laskaris, W. M. Snow, and C. B. Fu, Phys. Rev. D **85**, 031505 (2012), arXiv: 1203.3900.

11 R. Alarcon, J. Alexander, V. Anastassopoulos, T. Aoki, R. Baartman, S. Baeßler, L. Bartoszek, D. H. Beck, F. Bedeschi, R. Berger, M. Berz, H. L. Bethlem, T. Bhattacharya, M. Blaskiewicz, T. Blum, T. Bowcock, A. Borschevsky, K. Brown, D. Budker, S. Burdin, B. C. Casey, G. Casse, G. Cantatore, L. Cheng, T. Chupp, V. Cianciolo, V. Cirigliano, S. M. Clayton, C. Crawford, B. P. Das, H. Davoudiasl, J. de Vries, D. DeMille, D. Denisov, M. V. Diwan, J. M. Doyle, J. Engel, G. Fanourakis, R. Fatemi, B. W. Filippone, V. V. Flambaum, T. Fleig, N. Fomin, W. Fischer, G. Gabrielse, R. F. G. Ruiz, A. Gardikiotis, C. Gatti, A. Geraci, J. Gooding, B. Golub, P. Graham, F. Gray, W. C. Griffith, S. Haciomeroglu, G. Gwinner, S. Hoekstra, G. H. Hoffstaetter, H. Huang, N. R. Hutzler, M. Incagli, T. M. Ito, T. Izubuchi, A. M. Jayich, H. Jeong, D. Kaplan, M. Karuza, D. Kawall, O. Kim, I. Koop, W. Korsch, E. Korobkina, V. Lebedev, J. Lee, S. Lee, R. Lehnert, K. K. H. Leung, C.-Y. Liu, J. Long, A. Lusiani, W. J. Marciano, M. Maroudas, A. Matlashov, N. Matsumoto, R. Mawhorter, F. Meot, E. Mereghetti, J. P. Miller, W. M. Morse, J. Mott, Z. Omarov, L. A. Orozco, C. M. O'Shaughnessy, C. Ozben, S. Park, R. W. P. J. au2, A. N. Petrov, G. M. Piacentino, B. R. Plaster, B. Podobedov, M. Poelker, D. Pocanic, V. S. Prasannaa, J. Price, M. J. Ramsey-Musolf, D. Raparia, S. Rajendran, M. Reece, A. Reid, S. Rescia, A. Ritz, B. L. Roberts, M. S. Safronova, Y. Sakemi, P. Schmidt-Wellenburg, A. Shindler, Y. K. Semertzidis, A. Silenko, J. T. Singh, L. V. Skripnikov, A. Soni, E. Stephenson, R. Suleiman, A. Sunaga, M. Syphers, S. Syritsyn, M. R. Tarbutt, P. Thoerngren, R. G. E. Timmermans, V. Tishchenko, A. V. Titov, N. Tsoupas, S. Tzamarias, A. Variola, G. Venanzoni, E. Vilella, J. Vossebeld, P. Winter, E. Won, A. Zelenski, T. Zelevinsky, Y. Zhou, and K. Zioutas, arXiv: 2203.08103.

12 Y. Y. Jau, W. C. Chen, T. R. Gentile, and D. S. Hussey, Rev. Sci. Instrum. **91**, 073303 (2020).

13 N. Sachdeva, I. Fan, E. Babcock, M. Burghoff, T. E. Chupp, S. Degenkolb, P. Fierlinger, S. Haude, E. Kraegeloh, W. Kilian, S. Knappe-Grüneberg, F. Kuchler, T. Liu, M. Marino, J. Meinel, K. Rolfs, Z. Salhi, A. Schnabel, J. T. Singh, S. Stuiber, W. A. Terrano, L. Trahms, and J. Voigt, Phys. Rev. Lett. **123**, 143003 (2019), arXiv: 1909.12800.

14 J. M. Wild, N. J. Stewart, and H.-F. Chan, *Hyperpolarised Helium-3 (^{3}He) MRI: Physical Methods for Imaging Human Lung Function* (Springer International Publishing, Cham, 2018), pp. 69-97.

15 G. Collier, T. Pałasz, A. Wojna, B. Głowacz, M. Suchanek, Z. Olejniczak, and T. Dohnalik, J. Appl. Phys. **113**, 204905 (2013), arXiv: 1302.4863.

---

1) In our most recent tests of newly made smaller-sized cells, the T_2 value for the aluminosilicate cell was about 5 s. For the borosilicate cells, a T_2 value of up to 9 s was recorded. Both measurements were taken using the pickup coil method with the discharge turned off.

16 S. Karpuk, F. Allmendinger, M. Burghoff, C. Gemmel, M. Güldner, W. Heil, W. Kilian, S. Knappe-Grüneberg, C. Mrozik, W. Müller, E. W. Otten, M. Repetto, Z. Salhi, U. Schmidt, A. Schnabel, F. Seifert, Y. Sobolev, L. Trahms, and K. Tullney, Phys. Part. Nuclei **44**, 904 (2013).

17 W. T. Lee, G. Zheng, C. L. Talbot, X. Tong, T. D'Adam, S. R. Parnell, M. de Veer, G. Jenkin, G. R. Polglase, S. B. Hooper, B. R. Thompson, F. Thien, and G. F. Egan, Magn. Reson. Imag. **79**, 112 (2021).

18 S. Chen, Y. Lan, H. Li, L. Xia, C. Ye, X. Lou, and X. Zhou, Biomedicines **10**, 781 (2022).

19 H. Li, X. Zhao, Y. Wang, X. Lou, S. Chen, H. Deng, L. Shi, J. Xie, D. Tang, J. Zhao, L. S. Bouchard, L. Xia, and X. Zhou, Sci. Adv. **7**, eabc8180 (2021).

20 T. Okudaira, T. Oku, T. Ino, H. Hayashida, H. Kira, K. Sakai, K. Hiroi, S. Takahashi, K. Aizawa, H. Endo, S. Endo, M. Hino, K. Hirota, T. Honda, K. Ikeda, K. Kakurai, W. Kambara, M. Kitaguchi, T. Oda, H. Ohshita, T. Otomo, H. M. Shimizu, T. Shinohara, J. Suzuki, and T. Yamamoto, Nucl. Instrum. Meth. Phys. Res. Sect. A **977**, 164301 (2020), arXiv: 2005.14399.

21 W. C. Chen, T. R. Gentile, R. Erwin, S. Watson, Q. Ye, K. L. Krycka, and B. B. Maranville, J. Phys.-Conf. Ser. **528**, 012014 (2014).

22 Z. Salhi, E. Babcock, K. Bingöl, K. Bussmann, H. Kammerling, V. Ossovyi, A. Heynen, H. Deng, V. Hutanu, S. Masalovich, J. Voigt, and A. Ioffe, J. Phys.-Conf. Ser. **1316**, 012009 (2019).

23 H. Hayashida, T. Oku, H. Kira, K. Sakai, K. Hiroi, T. Ino, T. Shinohara, T. Imagawa, M. Ohkawara, K. Ohoyama, K. Kakurai, M. Takeda, D. Yamazaki, K. Oikawa, M. Harada, N. Miyata, K. Akutsu, M. Mizusawa, J. D. Parker, Y. Matsumoto, S. Zhang, J. Suzuki, K. Soyama, K. Aizawa, and M. Arai, J. Phys.-Conf. Ser. **711**, 012007 (2016).

24 C. Y. Jiang, X. Tong, D. R. Brown, S. Chi, A. D. Christianson, B. J. Kadron, J. L. Robertson, and B. L. Winn, Rev. Sci. Instrum. **85**, 075112 (2014).

25 C. B. Fu, T. R. Gentile, G. L. Jones, W. C. Chen, R. Erwin, S. Watson, C. Broholm, J. A. Rodriguez-Rivera, and J. Scherschligt, Physica B **406**, 2419 (2011).

26 E. Babcock, and A. Ioffe, Physica B **406**, 2448 (2011).

27 C. Jiang, AAPPS Bull. **33**, 21 (2023).

28 T. R. Gentile, P. J. Nacher, B. Saam, and T. G. Walker, Rev. Mod. Phys. **89**, 045004 (2017), arXiv: 1612.04178.

29 T. G. Walker, J. Phys.-Conf. Ser. **294**, 012001 (2011).

30 F. D. Colegrove, L. D. Schearer, and G. K. Walters, Phys. Rev. **132**, 2561 (1963).

31 E. Babcock, I. Nelson, S. Kadlecek, B. Driehuys, L. W. Anderson, F. W. Hersman, and T. G. Walker, Phys. Rev. Lett. **91**, 123003 (2003).

32 D. R. Rich, T. R. Gentile, T. B. Smith, A. K. Thompson, and G. L. Jones, Appl. Phys. Lett. **80**, 2210 (2002).

33 S. Yan, M. F. Zhang, W. C. Guo, W. Z. Wang, J. Gong, T. J. Liang, B. Q. Liu, M. Peng, S. M. Peng, G. A. Sun, X. Q. Tu, H. Y. Yan, J. H. Zhang, and H. Zheng, Sci. China-Phys. Mech. Astron. **62**, 102021 (2019).

34 Y. Zhan, X. Peng, S. Li, L. Zhang, J. Chen, and H. Guo, Appl. Phys. B **125**, 170 (2019).

35 M. Farooq, T. Chupp, J. Grange, A. Tewsley-Booth, D. Flay, D. Kawall, N. Sachdeva, and P. Winter, Phys. Rev. Lett. **124**, 223001 (2020).

36 A. Nikiel, P. Blümler, W. Heil, M. Hehn, S. Karpuk, A. Maul, E. Otten, L. M. Schreiber, and M. Terekhov, Eur. Phys. J. D **68**, 330 (2014), arXiv: 1405.6853.

37 D. Flay, D. Kawall, T. Chupp, S. Corrodi, M. Farooq, M. Fertl, J. George, J. Grange, R. Hong, R. Osofsky, S. Ramachandran, E. Swanson, and P. Winter, J. Inst. **16**, P12041 (2021), arXiv: 2109.08992.

38 A. Schneider, B. Sikora, S. Dickopf, M. Müller, N. S. Oreshkina, A. Rischka, I. A. Valuev, S. Ulmer, J. Walz, Z. Harman, C. H. Keitel, A. Mooser, and K. Blaum, Nature **606**, 878 (2022), arXiv: 2206.05943.

39 B. Abi, T. Albahri, S. Al-Kilani, D. Allspach, L. P. Alonzi, A. Anastasi, A. Anisenkov, F. Azfar, K. Badgley, S. Baeßler, I. Bailey, V. A. Baranov, E. Barlas-Yucel, T. Barrett, E. Barzi, A. Basti, F. Bedeschi, A. Behnke, M. Berz, M. Bhattacharya, H. P. Binney, R. Bjorkquist, P. Bloom, J. Bono, E. Bottalico, T. Bowcock, D. Boyden, G. Cantatore, R. M. Carey, J. Carroll, B. C. K. Casey, D. Cauz, S. Ceravolo, R. Chakraborty, S. P. Chang, A. Chapelain, S. Chappa, S. Charity, R. Chislett, J. Choi, Z. Chu, T. E. Chupp, M. E. Convery, A. Conway, G. Corradi, S. Corrodi, L. Cotrozzi, J. D. Crnkovic, S. Dabagov, P. M. De Lurgio, P. T. Debevec, S. Di Falco, P. Di Meo, G. Di Sciascio, R. Di Stefano, B. Drendel, A. Driutti, V. N. Duginov, M. Eads, N. Eggert, A. Epps, J. Esquivel, M. Farooq, R. Fatemi, C. Ferrari, M. Fertl, A. Fiedler, A. T. Fienberg, A. Fioretti, D. Flay, S. B. Foster, H. Friedsam, E. Frlež, N. S. Froemming, J. Fry, C. Fu, C. Gabbanini, M. D. Galati, S. Ganguly, A. Garcia, D. E. Gastler, J. George, L. K. Gibbons, A. Gioiosa, K. L. Giovanetti, P. Girotti, W. Gohn, T. Gorringe, J. Grange, S. Grant, F. Gray, S. Haciomeroglu, D. Hahn, T. Halewood-Leagas, D. Hampai, F. Han, E. Hazen, J. Hempstead, S. Henry, A. T. Herrod, D. W. Hertzog, G. Hesketh, A. Hibbert, Z. Hodge, J. L. Holzbauer, K. W. Hong, R. Hong, M. Iacovacci, M. Incagli, C. Johnstone, J. A. Johnstone, P. Kammel, M. Kargiantoulakis, M. Karuza, J. Kaspar, D. Kawall, L. Kelton, A. Keshavarzi, D. Kessler, K. S. Khaw, Z. Khechadoorian, N. V. Khomutov, B. Kiburg, M. Kiburg, O. Kim, S. C. Kim, Y. I. Kim, B. King, N. Kinnaird, M. Korostelev, I. Kourbanis, E. Kraegeloh, V. A. Krylov, A. Kuchibhotla, N. A. Kuchinskiy, K. R. Labe, J. LaBounty, M. Lancaster, M. J. Lee, S. Lee, S. Leo, B. Li, D. Li, L. Li, I. Logashenko, A. Lorente Campos, A. Lucá, G. Lukicov, G. Luo, A. Lusiani, A. L. Lyon, B. MacCoy, R. Madrak, K. Makino, F. Marignetti, S. Mastroianni, S. Maxfield, M. McEvoy, W. Merritt, A. A. Mikhailichenko, J. P. Miller, S. Miozzi, J. P. Morgan, W. M. Morse, J. Mott, E. Motuk, A. Nath, D. Newton, H. Nguyen, M. Oberling, R. Osofsky, J. F. Ostiguy, S. Park, G. Pauletta, G. M. Piacentino, R. N. Pilato, K. T. Pitts, B. Plaster, D. Počanić, N. Pohlman, C. C. Polly, M. Popovic, J. Price, B. Quinn, N. Raha, S. Ramachandran, E. Ramberg, N. T. Rider, J. L. Ritchie, B. L. Roberts, D. L. Rubin, L. Santi, D. Sathyan, H. Schellman, C. Schlesier, A. Schreckenberger, Y. K. Semertzidis, Y. M. Shatunov, D. Shemyakin, M. Shenk, D. Sim, M. W. Smith, A. Smith, A. K. Soha, M. Sorbara, D. Stöckinger, J. Stapleton, D. Still, C. Stoughton, D. Stratakis, C. Strohman, T. Stuttard, H. E. Swanson, G. Sweetmore, D. A. Sweigart, M. J. Syphers, D. A. Tarazona, T. Teubner, A. E. Tewsley-Booth, K. Thomson, V. Tishchenko, N. H. Tran, W. Turner, E. Valetov, D. Vasilkova, G. Venanzoni, V. P. Volnykh, T. Walton, M. Warren, A. Weisskopf, L. Welty-Rieger, M. Whitley, P. Winter, A. Wolski, M. Wormald, W. Wu, and C. Yoshikawa, Phys. Rev. Lett. **126**, 141801 (2021), arXiv: 2104.03281.

40 H. Iinuma, J. Phys.-Conf. Ser. **295**, 012032 (2011).

41 C. Talbot, M. Batz, P. J. Nacher, and G. Tastevin, J. Phys.-Conf. Ser. **294**, 012008 (2011).

42 M. Pinard, and F. Laloë, J. Phys. France **41**, 799 (1980).

43 P. J. Nacher, and M. Leduc, J. Phys. France **46**, 2057 (1985).

44 M. Abboud, A. Sinatra, X. Maître, G. Tastevin, and P. J. Nacher, Europhys. Lett. **68**, 480 (2004), arXiv: physics/0307154.

45 J. D. Maxwell, J. Alessi, G. Atoian, E. Beebe, C. S. Epstein, R. G. Milner, M. Musgrave, A. Pikin, J. Ritter, and A. Zelenski, Nucl. Instrum. Meth. Phys. Res. Sect. A **959**, 161892 (2020).

46 J. D. Maxwell, C. S. Epstein, and R. G. Milner, Nucl. Instrum. Meth. Phys. Res. Sect. A **764**, 215 (2014), arXiv: 1407.5654.

47 W. Lorenzon, T. R. Gentile, H. Gao, and R. D. McKeown, Phys. Rev. A **47**, 468 (1993).

48 F. Bloch, Phys. Rev. **70**, 460 (1946).

49 J. Dupont-Roc, M. Leduc, and F. Laloë, Phys. Rev. Lett. **27**, 467 (1971).

50 J. Dupont-Roc, M. Leduc, and F. Laloë, J. Phys. France **34**, 961 (1973).

51 J. Lee, *New Constraints on the Axion's Coupling to Nucleons from a Spin Mass Interaction Limiting Experiment (SMILE)*, Dissertation for Doctoral Degree (Princeton University, Princeton, 2019).

52 M. Auzinsh, D. Budker, and S. Rochester, *Optically Polarized Atoms: Understanding Light-Atom Interactions*, Dissertation for Doctoral Degree (Oxford University Press, Oxford, 2010).

53 W. Happer, Rev. Mod. Phys. **44**, 169 (1972).

54 H. Yan, K. Li, R. Khatiwada, E. Smith, W. M. Snow, C. B. Fu, P. H.

Chu, H. Gao, and W. Zheng, Commun. Comput. Phys. **15**, 1343 (2014), arXiv: 1305.3676.

55 M. V. Romalis, *Laser Polarized ^{3}He Target Used for a Precision Measurement of the Neutron Spin Structure*, Dissertation for Doctoral Degree (Princeton University, Princeton, 1997).

56 C. Gemmel, W. Heil, S. Karpuk, K. Lenz, C. Ludwig, Y. Sobolev, K. Tullney, M. Burghoff, W. Kilian, S. Knappe-Grüneberg, W. Müller, A. Schnabel, F. Seifert, L. Trahms, and S. Baeßler, Eur. Phys. J. D **57**, 303 (2010), arXiv: 0905.3677.

57 J. Ma, X. Wang, C. P. Sun, and F. Nori, Phys. Rep. **509**, 89 (2011), arXiv: 1011.2978.

58 L. Pezzé, A. Smerzi, M. K. Oberthaler, R. Schmied, and P. Treutlein, Rev. Mod. Phys. **90**, 035005 (2018), arXiv: 1609.01609.

59 H. Bao, J. Duan, S. Jin, X. Lu, P. Li, W. Qu, M. Wang, I. Novikova, E. E. Mikhailov, K. F. Zhao, K. Mølmer, H. Shen, and Y. Xiao, Nature **581**, 159 (2020).

60 J. Kong, R. Jiménez-Martínez, C. Troullinou, V. G. Lucivero, G. Tóth, and M. W. Mitchell, Nat. Commun. **11**, 2415 (2020).

61 R. Shaham, O. Katz, and O. Firstenberg, Nat. Phys. **18**, 506 (2022), arXiv: 2102.02797.

62 O. Katz, R. Shaham, and O. Firstenberg, Sci. Adv. **7**, eabe9164 (2021), arXiv: 2102.00229.

63 A. Serafin, M. Fadel, P. Treutlein, and A. Sinatra, Phys. Rev. Lett. **127**, 013601 (2021), arXiv: 2012.07216.